Acta Polytechnica CTU Proceedings **38**:573–578, 2022
https://doi.org/10.14311/APP.2022.38.0573

Published by the Czech Technical University in Prague

LAND USE CHANGE IMPACT ON URBAN LAND SURFACE TEMPERATURES: A GIS-SUPPORTED SATELLITE-BASED CASE STUDY

Caroline Walder, Pelin Firat Ors, Ardeshir Mahdavi*

TU Wien, Department of Building Physics and Building Ecology, Karlsplatz 13, 1040 Vienna, Austria
* corresponding author: amahdavi@tuwien.ac.at

Abstract. This paper illustrates the use of GIS techniques and satellite data in order to analyze the impact of land use change on the local urban microclimate. Specifically, a case study is presented that concerns the city of Vienna. Thereby, satellite-based images were used to classify the city of Vienna into four zones toward the computation of land surface temperatures in two reference years. The classified maps were then statistically projected into the future, resulting in predicted land surface temperatures. The findings highlight the relationship between urbanization and temperature rise in the urban context. The study used data from Landsat 8 satellite in 2013 and 2020. Land cover maps were generated with QGIS for past and current conditions and future land cover maps were projected and corresponding land surface temperatures were predicted. The analysis of satellite data highlighted land surface temperature increase in the city of Vienna. This rise in land surface temperatures correlates with urbanization-driven change in land use and land cover.

Keywords: Urbanization, land surface temperature, GIS, satellite data.

1. Introduction

Throughout the ongoing expansion and growth of urban areas and a current percentage of over 50 % of the world's population living in urban areas, the environment is expected to experience massive changes in the future. Due to this rapid increase of urbanization, cities are forced to use and therefore seal surfaces in order to provide enough space for their occupants [1]. Numerous cities already show higher air and surface temperatures than their rural surrounding areas, which is commonly known as the urban heat island (UHI) effect. The rise of intra-urban temperatures has a strong effect on the quality of life for humans, animals and on vegetation in general [2]. Furthermore, according to the Intergovernmental Panel on Climate Change (IPCC), world emissions would have to be cut by 45 % in less than ten years, in order to stay below the 1.5 K global warming threshold and to avoid a climate catastrophe [3]. Hence, the investigation of land use and land cover as well as quantifying their changes with regard to land surface temperature is of growing importance in urban development [4].

In this context, by projecting the land surface temperature (LST) in an urban setting from two scenarios into the future, the present contribution may contribute to the efforts toward a better understanding of the relationship between urbanization and urban thermal environment. Using the capital city of Austria, Vienna, as an example, the paper presents a GIS-based approach, starting from obtaining data from satellite images to a statistical analysis in order to predict future land surface temperature scenarios. The research thus aims to explore GIS techniques to obtain future land cover change projections. Moreover, the impacts of these projections on the urban thermal environment are evaluated through analysis of land surface temperatures.

2. Methodology

2.1. Study site and data

For the methodological part of the study, the city of Vienna was investigated regarding its climatic and geographical properties. Moreover, demographic characteristics of Vienna were considered, such as an average increase of the population growth of 0.8 %, which correlates to the city's rate of urbanization. By 2050, the city of Vienna is expected to have about 2.2 million inhabitants, which is an increase of about 16 % compared to 2020 [5].

Subsequently, the available satellite data was undergone a feasibility check in EarthExplorer, a service tool provided by the U.S. Geological Survey (USGS) [6, 7]. The Landsat 8 data belongs to the dataset "Landsat 8 OLI/TIRS C1 Level-1", which is a part of the "Landsat Collection 1 Level-1" data, courtesy of the U.S. Geological Survey [7, 8], for the representative years of 2013 and 2020 was evaluated with regard to cloud contamination, clarity issues, and other disturbances that might affect the image accuracy. The most suitable datasets recorded by Landsat 8 were acquired in World Reference System 2 (WRS-2) 190-026 for Vienna, with a maximum cloud coverage of 5 %. In order to mimic similar scenarios for past and present, respective Landsat 8 images were downloaded for early September in 2013 and 2020; courtesy of the U.S. Geological Survey [9]. The data was retrieved with

Semi-Automatic Classification Plugin (SCP) Version 7.0.0 in QGIS [10, 11], and covers a pixel size of 30 by 30 meters with an actual cloud coverage of below 1 %.

2.2. Land use/cover classification

Within the SCP environment in QGIS, the retrieved Landsat 8 images relevant to the study area were reduced in size and converted to reflectance maps. Converting the raw satellite imagery to obtain reflectance requires a metadata file, which was generated by retrieving the data from the USGS database. The metadata file contains the required information for the conversion. Secondly, the Dark Object Subtraction 1 (DOS1) atmospheric correction was applied to the reflectance images. For the resulting bands, the center wavelengths of Landsat 8 were defined manually [12]. For the classification of the images, training data was generated in QGIS. The "macro classes" chosen for the training input are water, built-up, vegetation, and bare soil. Within the macro classes, a more detailed separation was specified following rivers and lakes, buildings and roads, forests, and grassland, and low vegetated areas [12]. By applying "region growing algorithm", the "regions of interest" (ROI) were selected and assigned to the respective macro classes and classes according to the spectral distance, minimum size and maximum ROI width [12]. Ultimately, the training input file with 49 evenly distributed training input points was generated and applied to the 2013 and 2020 scenarios.

2.3. Land use/cover prediction

In order to predict the future land use/cover future scenario, Modules for Land Use Change Simulations (MOLUSCE) was applied in the study [13]. With an Artificial Neural Network (ANN), MOLUSCE is able to generate classified future land use/cover scenarios from past and present conditions. Due to the temporal difference of seven years between the two reference conditions, the simulation process with MOLUSCE was additionally executed five times after 2020, in order to reach the target year 2055. The projection was calculated with 5000 iterations and an inaccuracy of 0.1 %.

The past and present raster images were analyzed through an overlaying process on the land use/cover data. As a result, MOLUSCE creates a changes map, which identifies the changes of the land use/cover classification from past to present scenario. MOLUSCE is able to compute a transition matrix of the probability of change between the two given scenarios. The output of this algorithm is a transition potential raster of the model, i.e., certancy map, as well as the simulation results, which conclude the predicted future land use/cover classification [14].

2.4. Land surface temperature calculation

Calculating LST via the following workflow requires a set of input parameters that can be computed with the prepared satellite imagery. These parameters include emissivity (ε), which was derived through the "Normalized Difference Vegetation Index (NDVI) threshold method" as a first step. Based on the NDVI threshold method, emissivity can be derived for the 10 to 12 μm range [15, 16] which corresponds to Landsat 8, band 10 [15]. The mathematical base of the method is represented in Equation (1) [15–19].

$$\begin{aligned} &\varepsilon = \varepsilon_s \ for\ NDVI < NDVI_{min} \\ &\varepsilon = \varepsilon_v P_v + \varepsilon_s(1 - P_v) + d\varepsilon \\ &\qquad for\ NDVI_{min} \leq NDVI \leq NDVI_{max} \\ &\varepsilon = \varepsilon_v P_v + d\varepsilon \ for\ NDVI > NDVI_{max} \end{aligned} \tag{1}$$

In Equation (1), ε_s refers to the "soil" whereas ε_v refers to the "vegetation" emissivities [15–19]. Equation (2) gives the "vegetation proportion" based on minimum and maximum NDVI values [15–19].

$$P_v = \left(\frac{NDVI - NDVI_{min}}{NDVI_{max} - NDVI_{min}} \right)^2 \tag{2}$$

with $NDVI_{min} = 0.2$ and $NDVI_{max} = 0.5$ [15–19].

In Equation (3) below [15, 16, 19], F refers to "a shape factor" with a mean of 0.55 [19, 20].

$$d\varepsilon = (1 - \varepsilon_s)(1 - P_v)\ F\varepsilon_v \tag{3}$$

The calculation of emissivity can be concluded via Equation (4) [19].

$$\varepsilon = m\ P_v + n \tag{4}$$

with input parameters as per Equation (5) and (6) [19].

$$m = \varepsilon_v - \varepsilon_s - (1 - \varepsilon_s)\ F\varepsilon_v \tag{5}$$

$$n = \varepsilon_s + (1 - \varepsilon_s)\ F\varepsilon_v \tag{6}$$

Based on [19], the emissivity values can be assumed as $\varepsilon_v = 0.99$, $\varepsilon_s = 0.97$; and $m = 0.004$ and $n = 0.986$, resulting in Equation (7) [19]. Note that Equation (7) was proposed for Landsat 5 by [19] for the conditions of $NDVI_{min} \leq NDVI \leq NDVI_{max}$ and employed in the present work as a simple approach.

$$\varepsilon = 0.004\ P_v + 0.986 \tag{7}$$

The land surface temperature (LST) calculations were conducted following the workflow proposed by [15] which modified the "Mono-Window algorithm (MWA)" by [21] and adapted to Landsat 8 band 10 [15, 18]. This is given in Equation (8) below [15].

$$\begin{aligned} LST = \ &[a_{10}(1 - C_{10} - D_{10}) \\ &+ (b_{10}(1 - C_{10} - D_{10}))T_{10} - D_{10}T_a]\ /C_{10} \end{aligned} \tag{8}$$

where, $a_{10} = -62.7182$ and $b_{10} = 0.4339$ were employed in the present study [15], whereas C_{10} and D_{10} refer to the "internal parameters" (Equations (9) and (10)) [15].

$$C_{10} = \tau_{10}\varepsilon_{10} \tag{9}$$

$$D_{10} = (1 - \tau_{10})\left[1 + (1 - \varepsilon_{10})\,\tau_{10}\right], \tag{10}$$

where τ_{10} is the "atmospheric transmittance" and ε_{10} refers to the "ground emissivity". Both parameters are stated for Landsat 8, Band 10 [15].

The "effective mean atmospheric temperature" (T_a) can be estimated by the linear relation, based on the "near-surface air temperature" (T_0) and considering the atmospheric states of the location [15, 18, 21]. As per [15], T_0 can be derived from local meteorological stations and calculated by Equation (11) [15, 22].

$$T_{0,t} = T_{min} + (T_{max} - T_{min}) \sin\left(\pi \frac{t + t_{dl}/2 - 12}{t_{dl} + 2t_{T_{max}}}\right) \tag{11}$$

with T_{min} and T_{max} as "the daily minimum and maximum near surface air temperatures" [15], obtained from weather stations in and around Vienna [23].

T_0 was calculated and spatially interpolated for the past and present scenarios. On the other hand, brightness temperature, T_{10}, can be calculated from "band-specific thermal conversion constants" (K_1 and K_2), "spectral radiance" (L_λ), and "radiance rescaling factors" (M_i, A_i) [12, 24]. These values can be found in the respective metadata file [12, 24]. The mathematical definition for brightness temperature T_{10} and spectral radiance L_λ are provided in Equations (12) and (13) [12, 24].

$$T_{10} = \frac{K_2}{\ln\left((K_1/L_\lambda) + 1\right)} \tag{12}$$

$$L_\lambda = M_i Q_{cal} + A_i \tag{13}$$

According to [15], atmospheric transmittance (τ_{10}) can be estimated – for the present study – according to "mid-latitude summer" with a water vapor content range of 1.6–4.4 g/cm^2. This range was selected by following the Equations (14) and (15) [15].

$$w = w_{(0)}/Rw_{(0)} \tag{14}$$

$$w_{(0)} = (H \cdot E \cdot A)/1000 \tag{15}$$

In Equation (14), $w_{(0)}$ refers to the ground-level water vapor content ($\mathrm{g \cdot cm^{-2}}$) of the atmosphere, w refers to the total water vapor content ($\mathrm{g \cdot cm^{-2}}$) of the atmospheric column between the ground and the sensor, and finally, $Rw_{(0)}$ corresponds to the ratio between the ground-level and total water vapor content [15]. In Equation (15), the term H refers to the relative air humidity (%) observed at the surface, E refers to the saturation mix ratio (g/kg) at a certain air temperature between water vapor and air, whereas for that temperature, A denotes the air density (g/m^3) [15].

The input parameters for E and A according to the respective specific air temperatures were interpolated for the weighted air temperature of 26.1 °C and 67 % relative humidity for Vienna [25]. This resulted in E = 22.05 and A = 1.178 [15]. Rw(0) resulted in 0.6834, for mid-latitude summer [15].

2.5. Land surface temperature projection

The results of the LST calculations were statistically projected by using a linear regression line. The dependent variable is LST; the independent variable is time. For each of the approximately 460 000 observed pixels per raster image, two observed LST output values are available: past and present. Thus, the observed values were extrapolated for predicting the LST of the future scenario.

3. Results and Discussion

3.1. Land use/land cover

The results for the land use/cover (LULC) classification of the past and present scenario showed 3.7 % water area for both scenarios. Further, it resulted in 43.6 % and 47.2 % built-up area, 44.3 % and 43.9 % vegetated area, as well as 8.4 % and 5.2 % bare soil, respectively. The predicted scenario of 2055 resulted in a distribution of 3.6 % for water surfaces, 51.4 % built-up area, 40.5 % vegetated area, and 4.5 % bare soil. Figure 1 includes the LULC resulting maps. As Figure 1 indicates, the majority of the water surfaces are distributed over the Danube River and its branches and tributaries. It can be seen that the Danube River is separated by several built-up area "stripes", which can be identified as bridges. For all three conditions, the highest density of built-up area corresponds either to the city center or areas of residential or commercial use as well as traffic areas. Areas covered by forest displayed the highest level of vegetation. Other green areas, primarily covered with grass, were also identified within the city. The majority of bare soil areas was identified in the city's north and south parts. This distribution is in line with the agricultural land use in and around Vienna.

In comparison to 2013, the LULC classification of 2020 shows a slight densification of the built-up area in the city center as well as in the outer districts of the city. It further indicates a drastic decrease of the bare soil areas, especially in the northern part of the city. Both reference years showed a small amount of built-up classified spots, evenly distributed over the forest regions in the eastern and western parts of the city.

Regarding the future scenario, the water surface remained mostly the same and the built-up area increased significantly. The vegetated and bare soil areas experienced a decrease of 7.8 % and 13.1 %, respectively. The MOLUSCE algorithm "erased" the sparsely distributed small built-up areas in the eastern and western forest areas of the city and overall densified the vegetated and built-up areas.

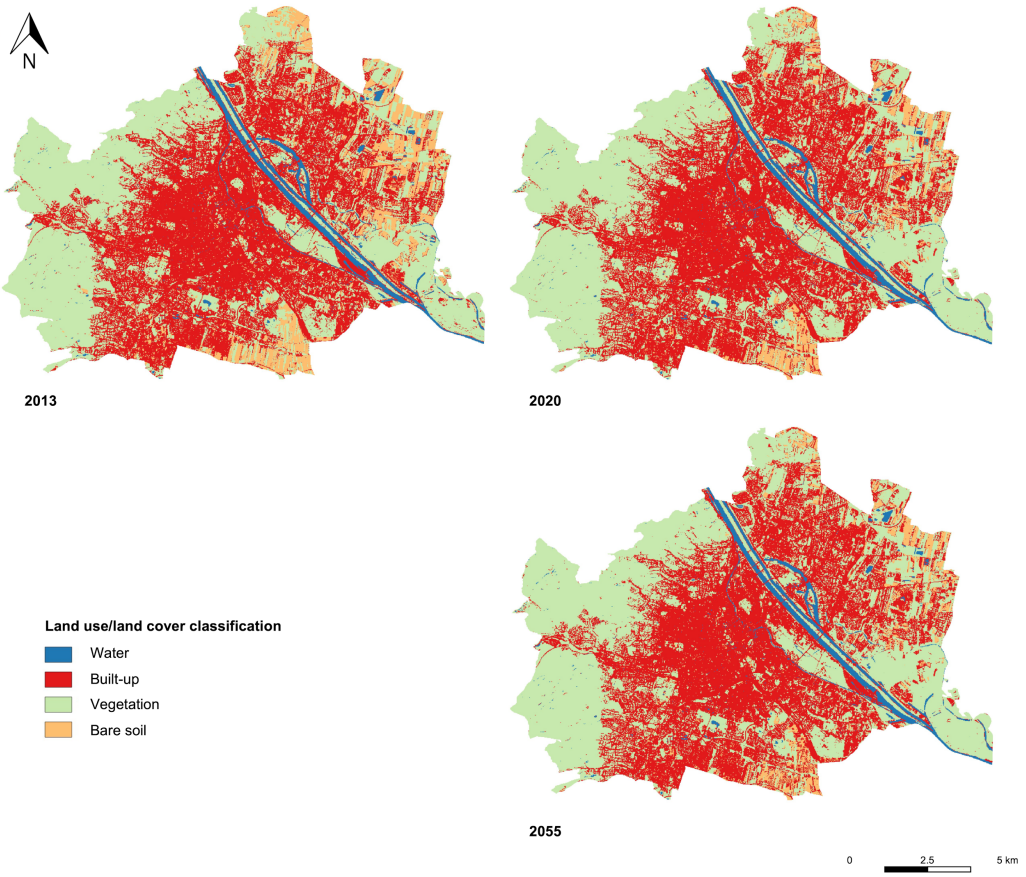

Figure 1. Land use/cover classification of Vienna.

	$\Delta T_{2020-2013}$ [K]	$\Delta T_{2055-2020}$ [K]
Min.	0.88	4.35
Mean	0.36	1.78
Max.	0.11	2.44

Table 1. Summary of the LST differences between 2020 and 2013 as well as 2055 and 2020 scenarios.

3.2. Land surface temperature

Table 1 summarizes the temperature differences (ΔT) between present and past as well as future and present scenarios for minimum, maximum and mean LSTs calculated over the study area. Figure 2 further presents the LST maps for the three scenarios pertaining to past, present and future conditions.

As indicated in Figure 2, the lowest temperatures for the past condition (i.e., 2013) can be obtained in the forest regions in the eastern and western parts of the city, as well as in the water area of the Danube River. It can be concluded that, additionally to the city center, the denser regions in the south show higher temperatures compared to their surroundings (Figure 2).

As already mentioned, the LST for the future scenario (2055) was not computed from the respective classified LULC map but projected based on a statistical (linear) extrapolation. The results indicate that the city center as well as the southern and north/northeastern parts experience significant increase in temperature over the course of the next 35 years. Not only the built-up areas show temperature rise, but also the eastern and western forest and grassland regions face higher surface temperatures.

3.3. Results evaluation

The classification result generated by MOLUSCE shows realistic values regarding the growing area of impervious surfaces. It appears plausible that bare soil areas, which in many cases are not only farmland but also unused and barren land, are going to be used for constructing new buildings and roadwork. However, it is possible that some inaccuracies occurred in the course of classifying the LULC of the future condition. For instance, MOLUSCE predicted single classified water pixels evenly distributed over the study site, where in reality no water bodies could be identified. It can be thus recommended that in future research efforts more spatial variables are included in the process of the MOLUSCE classification for better machine learning performance [14].

Although the results indicate a slight shift towards higher temperatures over time, it is nevertheless essential to interpret them with caution: First, as the cloud cover of the selected images were below 1 %, all pixels

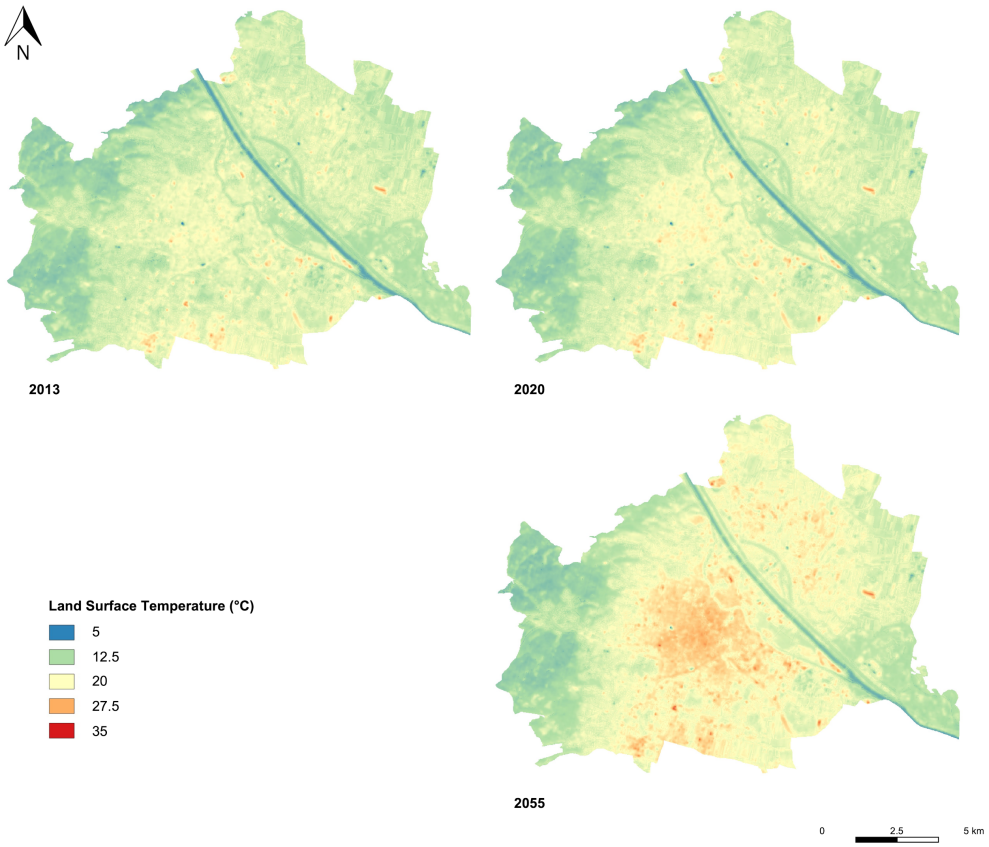

FIGURE 2. Land surface temperatures in Vienna.

within the images were considered as valid data points and an additional screening for cloudiness and potential quality issues was not performed. Also, although the satellite images were collected within a similar period in September of the respective years, the weather conditions might have been different. Therefore, it is plausible that these factors might have had an impact on the obtained outcomes. The calculated T_0 for the past and present scenario may also include irregularities due to the limited weather station data availability for the past scenario (two stations for 2013, seven stations for 2020). This limited information may account for inaccuracies in the later stages of the LST calculations. Moreover, the timing of Landsat 8 overpass in Vienna (10:45 a.m. CET) is not ideal for evaluating the urban thermal environment, as the thermal bands tend to peak between midday and the early afternoon [12]. In the present study, thermal data from Landsat 8 was selected considering its suitable spatial resolution [8]. Future studies may also employ readily processed LST products from various satellite sensors. One example may be the Aqua MODIS, which provides data with a coarser spatial resolution [26] but overpasses the study area around 12:30–13:30 p.m. CET. A recent LST product from Landsat (*Landsat Level-2 Surface Temperature Science Product courtesy of the U.S. Geological Survey*) [27] can also be an alternative that would shorten the workflow and ameliorate the mentioned limitations.

4. CONCLUSION

The key objective of this contribution was to explore an approach to predict land use/cover change and LST maps based on satellite imagery [28]. It can be seen from this effort that the utilization of satellite data provides a promising opportunity to predict future developments in the urban settings. The elaborated approach is not limited to the specific study area (Vienna), but can be applied to any setting on the urban scale, assuming that the required satellite images are publicly available. Further analyses could support the predictive assessment of future climatic conditions. Such analyses could include diurnal and seasonal variability in data acquisition. Utilizing data from a larger number of weather stations may also improve the LST calculations. These steps can facilitate the generalization of the approach pursued in this paper.

REFERENCES

[1] H. Ritchie, M. Roser. Urbanization, 2019. [2021-01-16]. https://ourworldindata.org/urbanization

[2] L. Yang, F. Qian, D.-X. Song, K.-J. Zheng. Research on urban heat-island effect. *Procedia Engineering* **169**:11–18, 2016. https://doi.org/10.1016/j.proeng.2016.10.002

[3] IPCC. Global warming of 1.5 °C. An IPCC Special Report on the impacts of global warming of 1.5 °C above pre-industrial levels and related global

greenhouse gas emission pathways, in the context of strengthening the global response to the threat of climate change, sustainable development, and efforts to eradicate poverty. [In press] [2022-02-04]. https://www.ipcc.ch/site/assets/uploads/sites/2/2019/06/SR15_Full_Report_High_Res.pdf

[4] A. Favretto. Urban heat island analysis with remote sensing and GIS methods: an application in the Trieste area (North-East of Italy). *Bollettino della Società Geografica Italiana* **1**(1):215–229, 2018. https://doi.org/10.13128/bsgi.v1i1.101

[5] Statistik Austria. Bevölkerung von Wien von 2010 bis 2020, 2020. [2020-08-05]. https://de.statista.com/statistik/daten/studie/317867/umfrage/prognose-zur-bevoelkerungsentwicklung-in-wien/#professional

[6] U.S. Geological Survey. USGS EarthExplorer, 2021. [2021-09-15]. https://earthexplorer.usgs.gov/

[7] U.S. Geological Survey, 2021. [2021-09-15]. https://www.usgs.gov/

[8] U.S. Geological Survey. USGS EROS Archive – Landsat Archives – Landsat 8 OLI (Operational Land Imager) and TIRS (Thermal Infrared Sensor) Level-1 Data Products, 2018. [Data products]. Courtesy of the U.S. Geological Survey. https://doi.org/10.5066/F71835S6

[9] U.S. Geological Survey. Landsat Collection 1 Level-1: Landsat 8 OLI/TIRS C1 Level-1: LC08_L1TP_190026_20130906_20200502_01_T1, LC08_L1TP_190026_20200909_20200918_01_T1, 2020. Landsat 8 images, courtesy of the U.S. Geological Survey (USGS). [2020-09-15]. https://earthexplorer.usgs.gov/

[10] L. Congedo. Semi-Automatic Classification Plugin: A Python tool for the download and processing of remote sensing images in QGIS. *Journal of Open Source Software* **6**(64):3172, 2021. https://doi.org/10.21105/joss.03172

[11] QGIS.org. QGIS Geographic Information System, 2021. [2020-09-15]. http://www.qgis.org

[12] L. Congedo. Semi-automatic classification plugin documentation, 2020. [2021-01-30]. https://readthedocs.org/projects/semiautomaticclassificationmanual/downloads/pdf/latest/

[13] NextGIS. Molusce, 2014. [2020-10-04]. https://github.com/nextgis/molusce

[14] Asia Air Survey, NextGIS. MOLUSCE Modules for Land Use Change Evaluation. Quick help, 2014. [2020-10-04]. https://github.com/nextgis/molusce/blob/master/doc/en/QuickHelp.pdf

[15] F. Wang, Z. Qin, C. Song, et al. An improved mono-window algorithm for land surface temperature retrieval from Landsat 8 Thermal Infrared Sensor data. *Remote Sensing* **7**(4):4268–4289, 2015. https://doi.org/10.3390/rs70404268

[16] J. A. Sobrino, J. C. Jiménez-Muñoz, G. Sòria, et al. Land surface emissivity retrieval from different VNIR and TIR sensors. *IEEE Transactions on Geoscience and Remote Sensing* **46**(2):316–327, 2008. https://doi.org/10.1109/TGRS.2007.904834

[17] J. A. Sobrino, N. Raissouni, Z.-L. Li. A comparative study of land surface emissivity retrieval from NOAA data. *Remote Sensing of Environment* **75**(2):256–266, 2001. https://doi.org/10.1016/S0034-4257(00)00171-1

[18] L. Wang, Y. Lu, Y. Yao. Comparison of three algorithms for the retrieval of land surface temperature from Landsat 8 images. *Sensors* **19**(22):5049, 2019. https://doi.org/10.3390/s19225049

[19] J. A. Sobrino, J. C. Jiménez-Muñoz, L. Paolini. Land surface temperature retrieval from LANDSAT TM 5. *Remote Sensing of Environment* **90**(4):434–440, 2004. https://doi.org/10.1016/j.rse.2004.02.003

[20] J. A. Sobrino. *Desarrollo de un modelo teórico para implementar la medida de la temperatura realizada mediante teledetección. Aplicación a un campo de naranjos*. Doctoral dissertation, University of Valencia, Valencia, Spain, 1989. ISBN 84-370-0598-1.

[21] Z. Qin, A. Karnieli, P. Berliner. A mono-window algorithm for retrieving land surface temperature from Landsat TM data and its application to the Israel-Egypt border region. *International Journal of Remote Sensing* **22**(18):3719–3746, 2001. https://doi.org/10.1080/01431160010006971

[22] R. Leuning, F. M. Kelliher, D. G. G. De Pury, E.-D. Schulze. Leaf nitrogen, photosynthesis, conductance and transpiration: scaling from leaves to canopies. *Plant, Cell & Environment* **18**(10):1183–1200, 1995. https://doi.org/10.1111/j.1365-3040.1995.tb00628.x

[23] J. Kachelmann. Kachelmannwetter., 2020. [2020-12-14]. https://kachelmannwetter.com

[24] U.S. Geological Survey. Landsat missions. Using the USGS Landsat level-1 data product., 2021. [2020-10-03]. https://www.usgs.gov/core-science-systems/nli/landsat/using-usgs-landsat-level-1-data-product

[25] Time and Date AS. Wetter in Wien, Wien, Österreich. [2020-12-14]. https://www.timeanddate.de/wetter/oesterreich/wien

[26] NASA. MODIS Moderate Resolution Imaging Spectroradiometer. [2022-02-04]. https://modis.gsfc.nasa.gov/data/

[27] M. Cook, J. R. Schott, J. Mandel, N. Raqueno. Development of an operational calibration methodology for the Landsat thermal data archive and initial testing of the atmospheric compensation component of a land surface temperature (LST) product from the archive. *Remote Sensing* **6**(11):11244–11266, 2014. https://doi.org/10.3390/rs61111244

[28] C. Walder. *Predicting land surface temperatures in urban areas from Landsat 8 images – A GIS-based approach*. Diploma thesis, Technische Universität Wien, 2021. https://doi.org/10.34726/hss.2021.80480